JOURNAL OF PROPULSION AND POWER
Vol. 22, No. 1, January–February 2006

Experimental Study of Confined, Swirling, Nonpremixed Gas Flame for Validation of Simulations

E. J. Tribbett,* C. M. Sipperley,* J.-Y. Huh,† C. F. Edwards,‡ and C. T. Bowman§
Stanford University, Stanford, California 94305-3032

An atmospheric-pressure, gaseous fuel combustor was developed to obtain data for validation of large-eddy or other high-fidelity simulations of confined combustor flow fields, such as found in gas-turbine engines. The air and fuel (methane) enter a constant-area combustor test section in separate concentric swirling jets through a 3:1 expansion. The test section is optically accessible, cylindrical in cross section, and four diameters in length. Measurements of two-component mean and rms velocity were obtained using laser Doppler velocimetry for both a combusting case and a nonreacting flow with identical inlet conditions. Measurements of major species (CO_2, CO, O_2, and hydrocarbons), minor species (NO), and mean temperature in the reacting flow were also obtained.

I. Introduction

VALIDATION of computational-fluid-dynamics (CFD) models for combustion flowfields requires suitable experimental results for comparison with model predictions. Although the literature contains a large number of combustion data sets, these are typically for unconfined jet flames, and so only a few are applicable to more complicated geometries such as gas-turbine-type combustors. To be useful for model validation in a gas-turbine combustor geometry, experiments are required with well-controlled and completely characterized inflow conditions, with a realistic confinement ratio, with controlled acoustic boundary conditions, and with a complete set of detailed velocity, gas temperature, and chemical species measurements. Of the available experimental studies on swirl-stabilized nonpremixed gas flames,[1–10,¶] none meets all of these requirements. Two ongoing studies[7–10,¶] have reported significant data sets that are suitable for model validation for flames with no confinement or with a large expansion ratio.

The objective of the present effort was to produce a database for a gaseous fuel combustor in a configuration resembling the primary zone of a gas turbine that would be suitable for testing reacting flow computations. Particular attention was paid to developing a test case with a compact, nonsooting flame and with well-defined inflow conditions and acoustic boundary conditions. To test chemistry submodels used in CFD codes, a lifted but stable flame was produced by coswirling the fuel and air and using a low-momentum fuel jet. Use of a lifted flame is an important feature of the present experiment both for realism (real combustors use lifted flames) and because of the challenge it presents to combustion modeling.

In this paper the design of the combustor and the operating conditions are described. Measurements of two-component mean and rms velocity are reported for a combusting case and for a nonreacting flow with identical inlet conditions. Measurements of major species (CO_2, CO, O_2, and hydrocarbons), minor species (NO), and mean temperature in the reacting flow also are reported, together with uncertainties in the measurements.

II. Experiment

A swirl-stabilized combustor that produces a compact, lifted flame was developed. Figure 1 is a schematic diagram of the combustor. It is composed of three sections: a flow development section, the test section, and a tail pipe. The flow development section consists of concentric fuel and air delivery tubes, which are fed with pressurized gases from a stagnation chamber. At the entrance to each delivery tube, there is a sonic choke that is used both to meter the gas and to provide a well-defined upstream acoustic boundary condition for the flow. Downstream from the inlet chokes, both delivery tubes have inline, helical swirlers through which the flow passes before entering the combustor.

To minimize bluff-body effects and avoid separation, traditional flat-blade swirlers were not used. Instead, a low-blockage swirler design based on curved channel flow design criteria was used to generate a swirling flow free of these effects (Fig. 2). The fins of the swirler separate the flow into regions that can each be approximated as a two-dimensional curved air channel. Each channel gradually transitions from a purely axial flow into a helical flow at the desired angle. The rate of transition is based on design criteria for turning vanes in wind tunnels so as to avoid separation on the back (suction) side of the blades. Maximizing the number of vanes reduces the risk of separation and more closely approximates a quasi-two-dimensional curved channel flow. Minimizing the number of vanes reduces the overall blockage of the swirler. Because of this tradeoff, the number of vanes was chosen to keep that gap height of the annular passage approximately equal to the spacing of the vane—producing a channel with an aspect ratio near unity. A similar swirler was designed for the fuel tube that minimizes the size of the central hub required to connect the vanes of the swirler. (A geometric description of the swirlers is contained in Appendix A.) To permit the flow to relax after generation of the swirl, the swirlers are positioned well upstream of the inlet to the test section (40 air-gap heights or fuel-tube radii). The fuel and airstreams are coswirled to provide a small liftoff of the flame from the fuel delivery tube.

Swirling flows are particularly sensitive to inlet asymmetries. A small deviation of the supply tubes from concentricity will produce a large asymmetry in the distribution of the air. For this reason, the combustor has independent positioning of the airstream choke and the exit location of the gas tube within the air annulus. This ensures that both the air delivery into the flow preparation section and the flow entering the test section are uniform in the azimuthal direction.

Certain laser-based measurement techniques are difficult to implement using curved glass windows (e.g., laser Doppler velocimetry). At the same time, other techniques (e.g., flow visualization) benefit from having the unimpeded optical access afforded by use of a cylindrical test section. To accommodate both requirements, the test section of the combustor is made up of two parts. One-half of the test section is comprised of flat-faced, fused-silica windows that

---

Received 16 July 2004; revision received 22 April 2005; accepted for publication 25 July 2005.

[*] Graduate Student Researcher, Department of Mechanical Engineering.

[†] Postdoctoral Fellow, Department of Mechanical Engineering.

[‡] Associate Professor, Department of Mechanical Engineering. Member AIAA.

[§] Professor, Department of Mechanical Engineering. Member AIAA.

[¶] Data available online at www.tu-darmstadt.de/fb/mb/ekt/tecflam/.

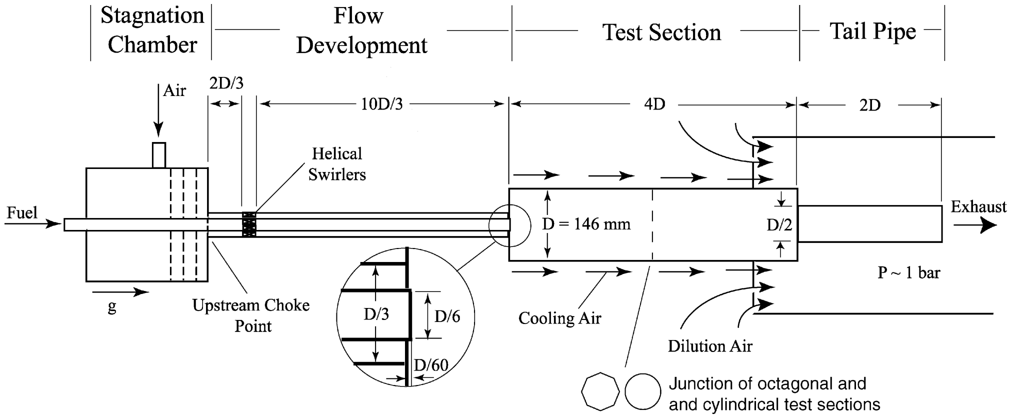

Fig. 1 Schematic diagram of the gas-fuel combustor.

Fig. 2 Photograph of the helical swirler for the air delivery tube.

Table 1 Design and operating conditions of the combustor

Condition	Value
Mass flow rate of air	30.7 ± 0.5 g/s
Mass flow rate of methane	1.20 ± 0.02 g/s
Firing rate	59 ± 1.0 kW
Equivalence ratio	0.67 ± 0.02
Mean velocity in air tube	23 m/s
Re (gap height) in air tube	14000
Mean velocity in fuel tube	3.9 m/s
Re (diameter) in fuel tube	5800
Momentum ratio (air/fuel)	153
Re (diameter) in combustor	5300
Gap height at air sonic choke	0.7 mm
Throat diameter at fuel sonic choke	2.16 mm
Combustor diameter (cylindrical section)	146 mm (D)
Combustor length	584 mm
Diameter of air tube	48.77 mm ($D/3$)
Inner diameter of fuel tube	23.7 mm ($D/6$)
Outer diameter of fuel tube	30.63 mm
Length of octagonal sectional of combustor	305 mm
Length of cylindrical section of combustor	273 mm
Swirler location from combustor inlet	487 mm ($10D/3$)
Swirler exit angle	45 deg
Average standoff height of the lifted flame	10 mm

form an octagonal cross section. This allows laser beams to enter without the focusing and redirection that would occur with curved windows. The octagonal shape was chosen to maintain a high degree of circular symmetry while still allowing significant optical access. The other half of the test section is made from a cylindrical quartz tube. The cross-sectional area of the octagon was chosen to match that of the cylindrical section. The two sections can be interchanged to allow any type of measurement to be made throughout the length of the combustor. For the majority of the data reported here, the octagonal test section was in the upstream position.

The exterior of the test section is cooled via forced convection from a concentric air shroud surrounding the combustor. Calculations were preformed to determine the deviation from a wall adiabatic condition because of the presence of this cooling air and radiative losses from the combustion gases. Temperature and axial-velocity profiles at a downstream location in the combustor were integrated to obtain an enthalpy flux past this location. The mean temperature rise of the cooling airstream was also measured at this location to corroborate the results of the enthalpy flux calculation. These calculations indicate that 5–10% of the total heat release is lost to the cooling airstream or by radiation to the surroundings by the end of the primary combustion zone (187.6 mm downstream of the combustor inlet). Because of uncertainties in the data, particularly near the combustor wall (where there is a significant temperature deficit and a large portion of the total mass flux), a more precise estimate of the heat loss in the primary combustion zone cannot be provided.

The combustor is terminated by an exhaust section (tail pipe) of a smaller diameter than the test section. The exhaust contraction produces a positive pressure gradient to combat the tendency of swirling flows to have long vortex cores that can entrain air from outside of the combustor. The combustor operating conditions were chosen to provide a high-intensity, compact but lifted flame without significant acoustic excitation. (Operating conditions with significant acoustic activity were identified, but these conditions were not chosen for investigation in this study.) Details of the geometry and operating conditions are listed in Table 1, whereas Fig. 3 is a photograph of the flame taken during development.

For the laser Doppler velocimetry (LVD) measurements, a probe volume of ~100 μm diam and ~1 mm length is used, and the fuel and airstreams entering the upstream plenums are independently seeded with submicron Al_2O_3 particles. The seeding rates of the two streams are adjusted so that the flows entering the combustor have equal seed number density (as evidenced by velocity-normalized data rate). Also, for facilitating LDV measurements, the fuel tube is configured to protrude slightly (D/60) into the test section. This permits access to the fuel jet by the LDV beams, but does not significantly alter the structure of the flow. Sampling was performed over a period greater than 1000 integral timescales (45 s) or, in low data-rate regions, until 1000 samples had been obtained.

For temperature and stable species measurements, one window of the octagonal test section was replaced with an uncooled metal panel that permits insertion of a thermocouple probe or a water-cooled, stainless-steel, gas-sampling probe. The temperature was measured using an uncoated Pt-Pt 13% Rh thermocouple, with a nominal bead diameter of 300 μm. The thermocouple data were corrected for radiation using the measured velocity and species concentrations. The gas-sampling probe was operated with a suction velocity approximately equal to the bulk gas velocity in the combustor. This is estimated to produce a sampling volume with characteristic dimensions of the same order as the probe tip (~2 mm). All species measurements are reported on a dry basis with the exception of

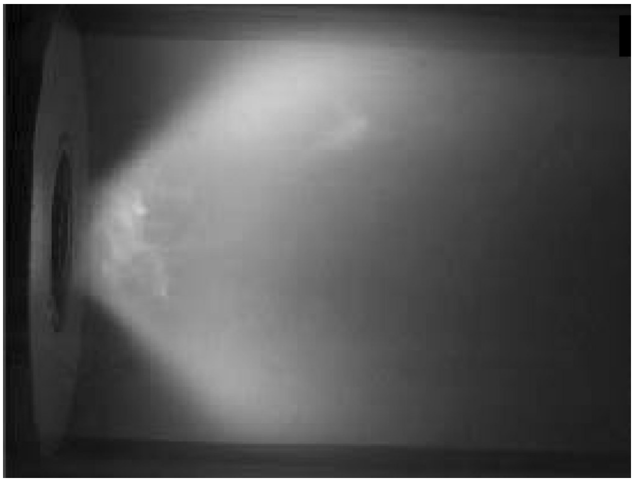

Fig. 3 Photograph of the gas-phase (methane) combustor during prototype testing (long-duration exposure). The flame is highly turbulent and lifted from the fuel delivery tube.

hydrocarbons. The O_2 mole fractions were measured using a paramagnetic analyzer. The CO and CO_2 mole fractions were measured using nondispersive infrared analyzers. The hydrocarbon (HC) mole fractions were measured using a heated flame ionization detector. The NO and NO_2 mole fractions were measured using a chemiluminescent analyzer, with an averaging time of 10 s. Measurement of other species took on the order of 30 s to reach a stable reading after positioning the probe. The gas-sampling probe was cooled with water from a temperature-controlled bath that was maintained near 70°C in order to prevent water condensation in the probe. Depending on the location of the probe in the combustor, the exit temperature of the cooling water varied from just over the inlet temperature to near the boiling point.

III. Results

A. Reacting Flow

All of the data are reported in tabular form in Appendix B.[¶] Figure 4 shows the inlet velocity profiles, while Figs. 5–10 present the streamwise development of the reacting flowfield. In these figures, the dark dashed line is the combustor centerline.

To define the combustor inflow conditions, measurements were made of three velocity components and their fluctuations near the inlet of the combustor. This measurement plane is located 4.5 mm from the upstream wall of the test section and was chosen because it is the first location that can be accessed by the LDV beams across the full width of the inlet flow. The data show relatively large axial- and azimuthal-velocity components across the air jet (note the difference in scale between the mean and rms plots), but a much smaller mean radial velocity (of the same order as the rms), indicating that the jet has not yet spread. The rms velocities of the three components for the air jet are similar to one another—consistent with an inertially dominated jet that has not yet felt much downstream influence. This is not the case with the fuel jet. Here, the mean axial-velocity component is still largest, but the radial and azimuthal components are nearly identical, indicating a strong radial divergence of the streamlines. Similarly, the rms azimuthal and radial velocities are nearly identical, and both are about one-third of the axial value, indicating a strong anisotropy at this location. This anisotropy is ascribed to the influence of the central recirculation zone. Because the interface between the incoming fuel jet and this recirculation zone is a stagnation point in the flow, displacement of this point in the streamwise direction ("bobbing" of the flame) can lead to significantly enhanced fluctuations in the axial-velocity component.

Figures 5 and 6 show the mean and rms of the axial and azimuthal components of velocity, respectively, throughout the reacting flowfield. Profiles are shown at eight stations ranging from 4.5 mm from the inlet plane to 325 mm downstream of that plane.

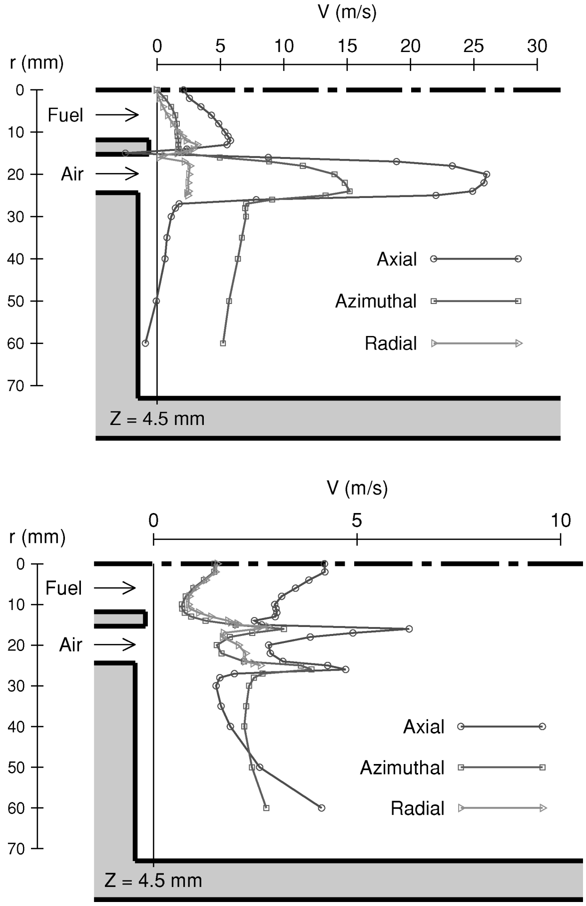

Fig. 4 Inlet (*Z* = 4.5 mm) mean (left) and rms (right) velocity profiles.

(An additional plane of radial velocity data is available at 3.5 mm from the entrance plane. Because of optical-access constraints, this was the only location where radial velocity data could be obtained across the region of interest in the flowfield. These data are not shown in Figs. 5 and 6 but are included in the tables in Appendix B.) Data were not acquired at further distances downstream because the flow was found to have little structure past 300 mm. No data are reported at planes between ∼200 and 300 mm because this region was not accessible to the LDV optics.

As previously stated, air enters the combustor with relatively large axial- and azimuthal-velocity components, and the rms velocity fluctuation is an order of magnitude lower than the mean. The fuel enters at lower velocity to provide a strong central recirculation zone (corresponding to the high momentum ratio of the flow) and with significant fluctuations such that the rms velocity is of the same order as the mean. As evident in the axial-velocity data, the air jet spreads rapidly outward toward the wall of the combustor, and a central recirculation zone (with a length approximately equal to the combustor diameter) is formed near the centerline. By the 43.8-mm measurement station, the rms fluctuation has become of the same order as the mean velocity at all radii, and the rms exceeds the mean near the rear stagnation point of the central recirculation zone ($Z \sim 150$ mm). Also evident in the axial-velocity data at 43.8 mm is an external recirculation zone adjacent to the upstream wall of the combustor.

Figures 7 and 8 show mean gas temperature and carbon dioxide and oxygen (dry basis) as functions of position in the flow. The temperature profiles are consistent with the spreading and mixing of the cold air jet and the presence of hot internal and external recirculation zones. The peak temperature is found in the central recirculation zone and is just below 2000 K. The carbon-dioxide and oxygen data also show the spreading of the air jet (as evidenced by the oxygen profiles) and presence of products in the recirculation zones (as evidenced by the carbon-dioxide profiles). The temperature and species profiles are essentially featureless past 200 mm downstream of the inlet plane.

[¶] Data available online at http://navier.stanford.edu/combustor_data.

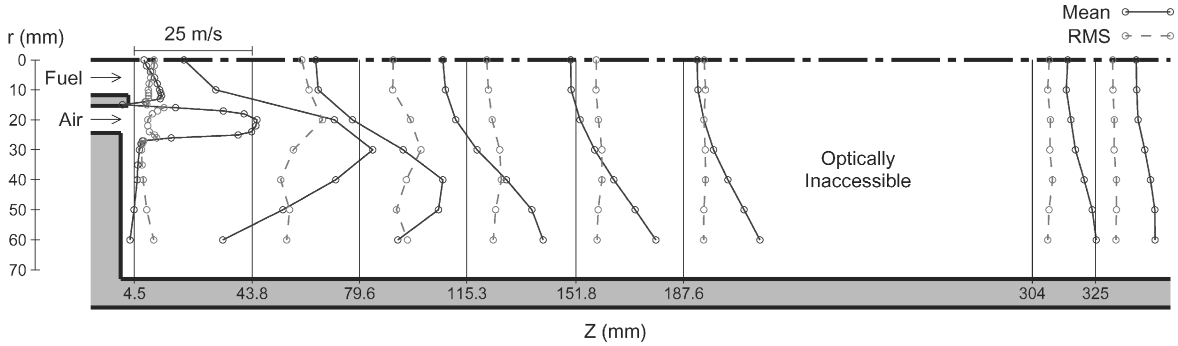

Fig. 5 Axial mean and rms velocity as a function of position in the reacting flow.

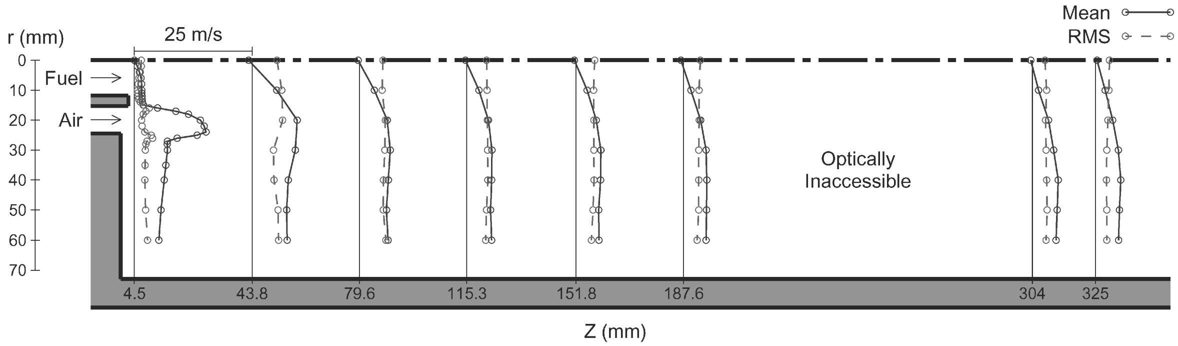

Fig. 6 Azimuthal mean and rms velocity as a function of position in the reacting flow.

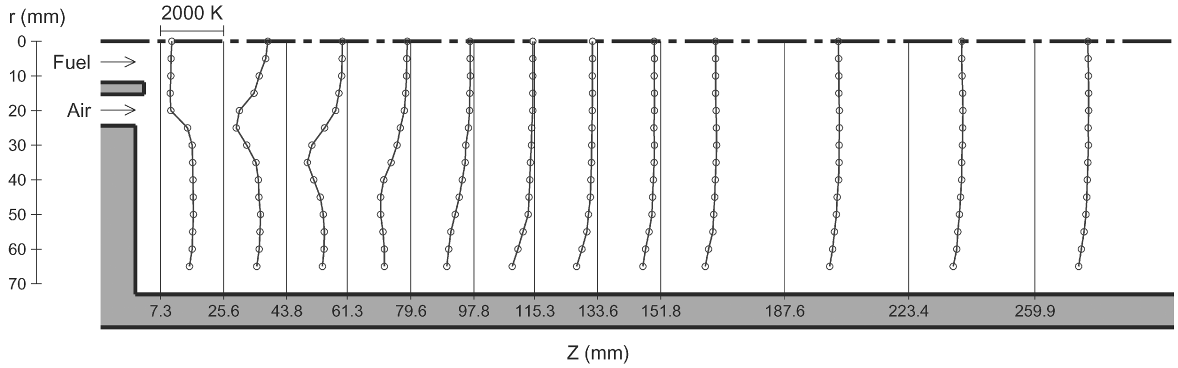

Fig. 7 Mean temperature as a function of position in the flame (uncoated 300-μm-diam bead, radiation corrected).

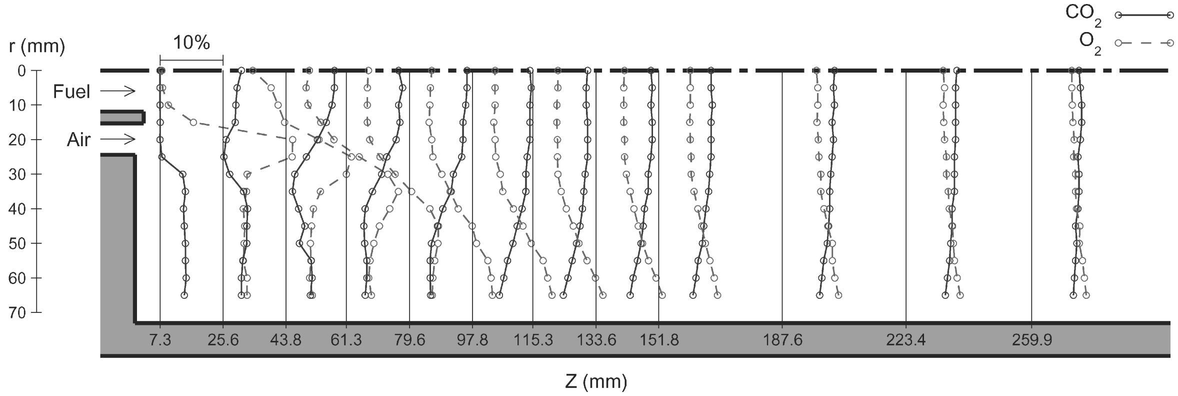

Fig. 8 CO_2 and O_2 as a function of position in the flame (mole percentage, dry basis).

Figure 9 shows profiles of hydrocarbons (reported as %C on a wet basis) and carbon monoxide (dry basis). Data are not reported for hydrocarbons in the central portion of the fuel jet at the two locations nearest the inlet because the concentration exceeds the measurement capabilities of the analyzer. The oxidation of fuel (hydrocarbons) to carbon monoxide is apparent, followed by subsequent disappearance of the carbon monoxide as it is converted to carbon dioxide. Also evident is the spreading of the fuel jet in the radial direction along the inner edge of the air jet. This spreading is most easily seen by comparing the oxygen profiles in Fig. 8 with the hydrocarbon profiles in Fig. 9.

The nitric-oxide profiles are shown in Fig. 10. The highest concentrations of nitric oxide are found on the centerline. The peak value occurs near the middle of the central recirculation zone, but then slowly decreases as the recirculation zone closes and the flow proceeds downstream.

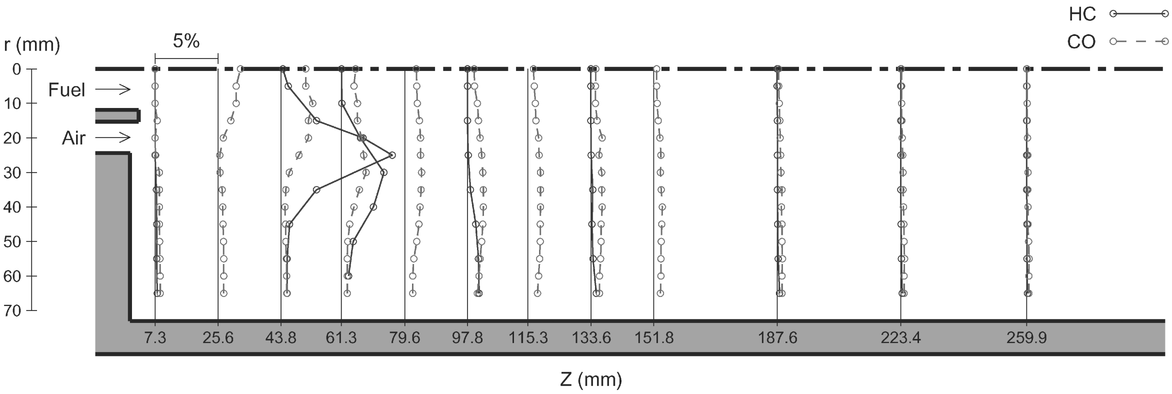

Fig. 9 CO (mole %, dry basis) and hydrocarbons (mole % as methane, wet basis) as a function of position in the flame.

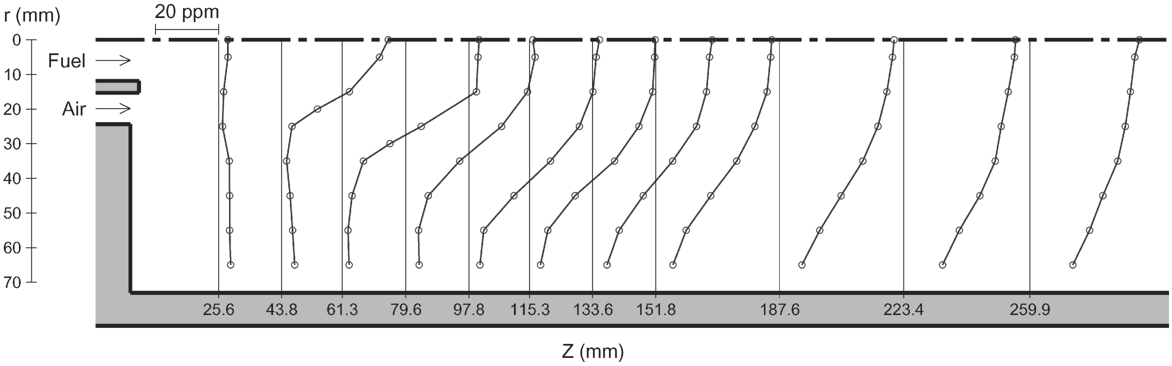

Fig. 10 NO as a function of position in the flame (mole ppm, dry basis).

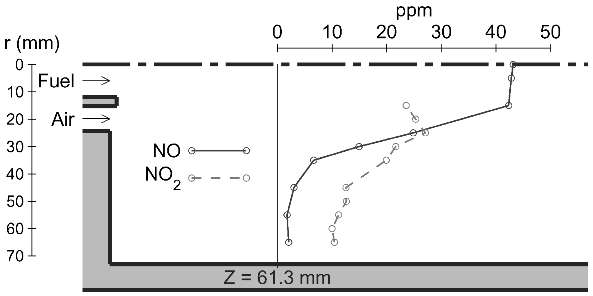

Fig. 11 NO and NO_2 mole fraction profiles at Z = 61.3 mm (mole ppm, dry basis).

Significant levels of nitrogen dioxide, NO_2, often are found on the air side of diffusion flames.[11] To establish the relative concentrations of nitric oxide and nitrogen dioxide in the initial regions of the combustor, a radial profile of NO_2 was obtained at the 61.3 mm plane. Figure 11 shows the measured NO and NO_2 profiles at this axial location. The NO_2 peaks at a radial position of about 25 mm, which is near the edge of the hot recirculation zone. At this radial location the measured NO_2 concentrations are comparable to NO. In the cooler regions outside of the recirculation zone, the NO_2 mole fractions exceed the NO mole fractions. At further downstream locations, the gas temperature is sufficiently high so that any NO_2 formed is rapidly dissociated to form NO so that the reported NO measurements can be viewed as total NOx.

B. Nonreacting Flow

To assist in the application of CFD to the present flow configuration, limited LDV data were acquired under cold-flow conditions. These conditions correspond to the same flow rates of methane and air as used in the reacting flow experiment. Figures 12 and 13 show the axial- and azimuthal-velocity components, respectively. Although the profiles near the inlet are similar to those for the reacting flow case, they are not identical. The air jet appears to spread more quickly than in the combusting case. No data are reported in the region of the flow marked as being bistable. This is because this region was found to have bistable velocity statistics that we ascribe to the presence of a Coanda effect of the walls.[12] Examination of high-data-rate LDV records shows that the flow in this region alternates between mean values, but that these shifts occur at a sufficiently low frequency so that it was considered impractical to attempt to sample this part of the flowfield over a sufficient period of time to obtain stable statistics. A final feature to be noted in the cold flow is the emergence of an axial-velocity peak near the centerline well downstream of the central recirculation zone.

IV. Confidence Intervals

Confidence intervals were developed to facilitate comparison of the data with simulations. These confidence intervals about the mean values are reported in Appendix B. These intervals incorporate contributions associated with asymmetry, probe effects, set-point precision, as well as absolute error (accuracy).

The data at each axial station are reported as a function of radial position. Symmetry checks were made for each type of measurement, and it was found that uncertainties caused by asymmetry were smaller than other uncertainties in the measurements. Figure 14 illustrates the symmetry of the flow, showing axial-velocity data taken at two axial stations. At the inlet plane, the results of two separate scans of axial velocity across two different radii are superposed. It is apparent that the data lie on essentially the same curve. At the second plane, located where there is substantial structure in the flow, data are shown from a full diametral scan, but with the values for a part of the scan folded back to their corresponding radii. Again a high degree of symmetry is noted. All of the data lie within the recommended uncertainty band.

For the LDV data, where the rms variation of velocity has been measured, a confidence interval for the mean was established using the rms values as a basis. For the temperature and species measurements—where information about the sampling distribution is not available—confidence intervals were estimated directly from an uncertainty analysis of the measurement technique and the experimental assessments of reproducibility and symmetry of the flowfield. For this purpose a 50% confidence interval was chosen because it was felt that a more precise interval could not be justified.

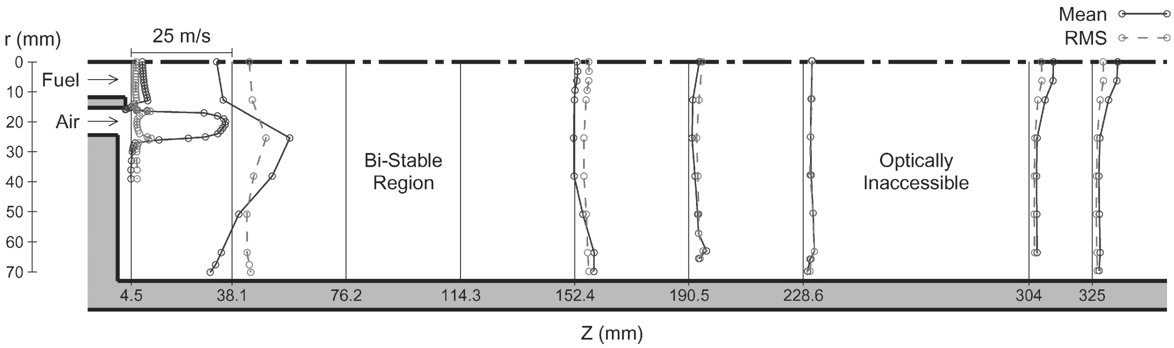

Fig. 12 Axial mean and rms velocity as a function of position in the cold flow.

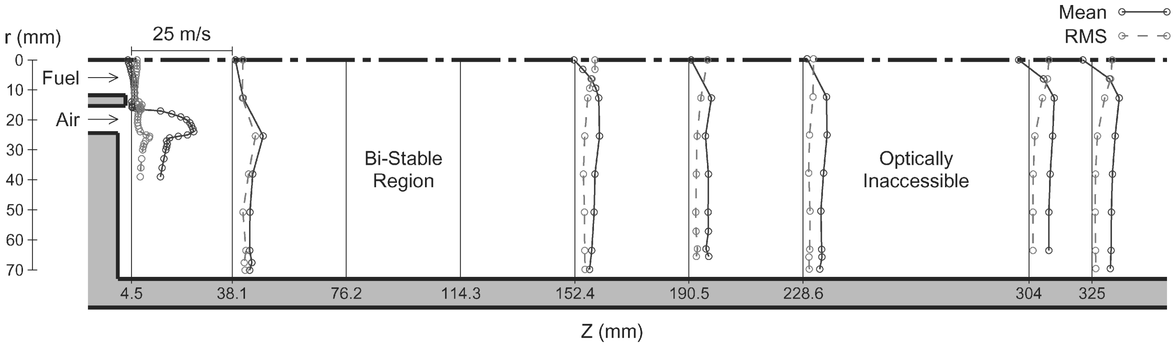

Fig. 13 Azimuthal mean and rms velocity as a function of position in the cold flow.

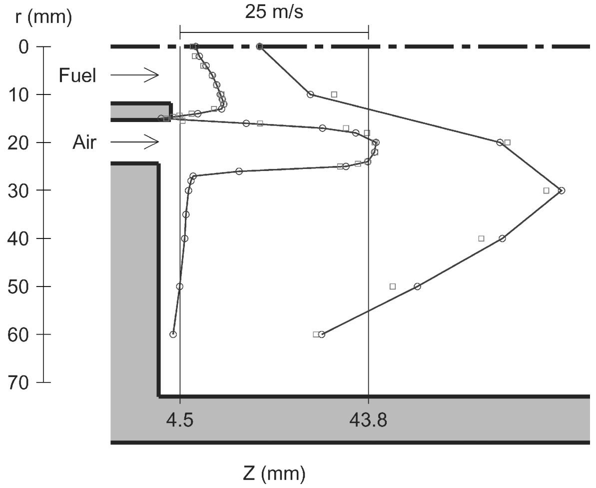

Fig. 14 Illustration of flow symmetry at the inlet plane (*Z* = 4.5 mm) and across the central recirculation zone (*Z* = 43.8 mm): ○, □, axial-velocity data from scans along different radii.

These confidence intervals represent possible deviations from true values, and, although repeatability has been included in the intervals, it should be noted that repeatability is generally much better than the intervals indicate. In other words, the precision of the measurements is most likely significantly better than is reflected in the bands reported, which are dominated by uncertainty in absolute accuracy.

Several sources of uncertainty are common to all of the measurements, whereas others are specific to individual techniques. Misalignment of the air and fuel tubes can significantly impact the flowfield. Another source of uncertainty common to the various measurements arises from possible misalignment of the probe within the combustor. Small errors (<1 mm) in the reported probe location become significant in regions of the flow with steep gradients. A final common source of uncertainty arises from the flow disturbance caused by the presence of a probe in the flowfield that will be most important in the recirculation zone. Because the magnitude of probe effects were largely qualitative, tighter confidence intervals could not be justified for the probe-sampled data.

For the velocity data, the rms velocity values are used as the 50% confidence interval about the mean. The mean values reported are the arithmetic average of all seed-particle arrivals. No correction was made for velocity biasing or density weighting. For purposes of comparison of the data with simulations, these effects can be accounted for by correcting the computational results before comparison is made (e.g., by using Favre-weighted velocity statistics). There are two primary uncertainties specific to the LDV measurements. First, the finite probe volume (beam crossing) will introduce error, particularly in regions of the flow with large velocity gradients. A slight asymmetric overlap of the beams in the probe volume can also introduce a systematic velocity bias. These effects are expected to be largest in regions of the flow with high rms velocities and steep gradients in velocity. Although care was taken to seed the cold air and fuel flows to the same mean number density, variations in seed density can cause additional error in the mixing layer between the two flows. Long data sets were taken to eliminate the possibility that very low-frequency variations in velocity would not be captured. Although this could be accomplished everywhere in the case of the combusting flow, there is a bistable region in the cold-flow case where it was not practical to meet this requirement. Velocity data are not reported for this region.

Three major effects were considered in determining appropriate confidence intervals for the temperature data. First, low-frequency fluctuations in the temperature observed on the thermocouple display were considered. Second, the uncertainty associated with the radiation correction of the thermocouple data was considered. The correction requires that the average Nusselt number over the thermocouple bead be evaluated in terms of an appropriate Reynolds number. In regions of the flow where the rms velocity is high compared to the mean velocity, the rms velocity was used to estimate the Reynolds number. While this radiation correction contributes uncertainty in all areas of the combustor, it dominates other uncertainties in regions with very low ratios of mean velocity to rms velocity and high temperatures. The final consideration in the temperature uncertainty analysis was the nonlinear averaging of the higher-frequency temporal variations in temperature. In some regions of the flow, the flame front continually moves back and forth across the bead, exposing it to large fluctuations in temperature. Uncertainty regarding the averaging of this temperature variation can only be considered qualitatively, but is suspected to be significant in the first third of the combustor. Other sources of uncertainty such as variation of the thermocouple material properties and errors associated with the calibration of the display are small in comparison to the errors just discussed and were omitted from consideration. These effects were taken to be independent, and the associated uncertainties were added as independent components of an uncertainty vector.

Each gas analyzer has error bands reported by the manufacturer. These errors are generally small in comparison to uncertainties associated with the effects just described. Additional sources of uncertainty were considered for the carbon monoxide (CO), carbon dioxide (CO_2), nitric oxide (NO), and nitrogen dioxide (NO_2) data. It is common for non-dispersive infrared analyzers such as those used to measure CO and CO_2 to exhibit a beat frequency between the chopper and oscillator. This causes a small fluctuation about the mean reading that must be incorporated into the uncertainty. Calibration curves were also generated to interpret the readings obtained from the CO and CO_2 analyzers. In some regions, the slope (change in mole fraction per change in voltage reading) is quite large, increasing the uncertainty of the reported values.

There are several uncertainties specific to the NO_x analyzer. In some regions of the flow, the average readings from the analyzer fluctuated significantly, and, therefore, averaging effects associated with these fluctuations dominate the overall uncertainty. The analyzers were calibrated using NO and NO_2 in N_2. Variations in quenching efficiencies between N_2 and combustion products were considered, but generally found to be very small compared to other uncertainties. The uncertainties in the measured NO_2 mole fractions are comparatively large (with respect to the NO values). This is because it is known that NO_2 can be removed from the sample in the cold trap, desiccant and pump.

V. Summary

A set of mean and rms velocity profiles, mean stable species (CO_2, CO, O_2, and hydrocarbons) profiles, and mean gas temperature profiles have been obtained in a swirling methane-air turbulent diffusion flame in a confined configuration that resembles the primary zone of a gas turbine combustor. The inlet conditions of the combustor were carefully documented. An uncertainty analysis was performed for all of the measurements. A companion set of measurements was taken for a nonreacting flow with identical inlet conditions as the combusting flow. The data sets serve as a test case for reacting flow simulations. Additional studies under reacting spray flow conditions have recently been completed and will be reported in a subsequent paper.

Appendix A: Geometric Description of Fuel and Air Swirlers

The air swirler is shown in Fig. 2 in the text (left-hand swirl pointing downstream). The fuel swirler has the same sense swirl to delay mixing and enhance flame liftoff. The air and methane swirlers are of similar design. Each consists of 12 identical blades designed to avoid separation of the flow. The upstream edge of each blade is oriented normal to the purely axial incoming flow. The blades then curve, transitioning to a helix at the half-way point.

Table A1 Diameter and gap height for fuel and air swirlers

Swirler	D_{inner}, mm	D_{outer}, mm	D_{eff}, mm	g_h, mm
Fuel	10.00	23.77	18.6	7.15
Air	30.63	48.77	40.6	8.98

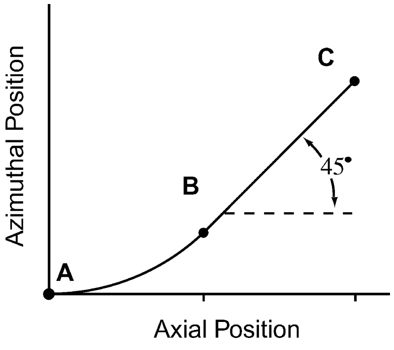

Fig. A1 Axial position as a function of azimuthal position at swirler effective diameter.

The pitch of flat helical blades can only be properly defined at one diameter (as opposed to continuously variable geometry blades on a propeller). We have chosen to define that diameter at the 50% area split of the annular region (see Table A1). The curve in Fig. A1 represents the azimuthal position as a function of axial position of each blade at the effective diameter D_{eff}. Point B represents the transition from the curved front half of the blades to the helical back half.

A cross section of the swirlers would show that the blades are pure radial extrusions. In other words, the mill bit used to cut the geometry was always mounted normal to the metal stock. The blades themselves are 1 mm thick measured normal to the local blade direction (as opposed to azimuthally). Finally, the outlet ends of the blades are not truncated normal to the helical curve but normal to the major axis of the annular region (tapered at an angle).

Curve A-B:

$$y_{AB} = 4\sqrt{2}g_h - \sqrt{32g_h^2 - x^2}$$

Line B-C:

$$y_{BC} = x - 4g_h\left(2 - \sqrt{2}\right)$$

Appendix B: Tabulated Data

Table B1 Axial (*Vz*) and radial (*Vr*) entrance velocity mean and rms as a function of position in the methane flame

r, mm	Vz, m/s	$VzRMS$, m/s	Vr, m/s	$VrRMS$, m/s
		Z = 3.5 mm (radial scan)		
0	2.07	4.00	−0.36	1.65
1	2.28	4.11	−0.17	1.64
2	2.88	3.89	0.19	1.47
3	3.61	3.95	0.48	1.31
4	3.93	3.38	0.85	1.21
5	4.39	3.16	1.00	1.11
6	4.85	3.00	1.29	0.92
7	5.04	2.89	1.48	0.90
8	5.04	5.11	1.74	0.90
9	5.27	2.74	2.04	0.97
10	5.57	2.87	2.36	1.24
11	4.47	2.61	3.13	1.74
12	0.33	2.48	1.57	2.68
13	−2.55	2.62	0.61	2.79
13.31	−1.27	3.57	−0.09	3.51
13.69	5.25	5.62	−1.32	3.58
14	10.07	5.82	−0.71	2.97
14.46	18.49	5.22	1.17	2.12
15	21.10	4.41	1.65	1.91
16	23.50	3.83	1.95	1.84
17	24.30	2.92	1.93	2.06
18	24.30	2.89	1.81	2.21
19	24.10	3.05	1.96	2.34
20	23.90	3.34	1.79	2.37
21	21.80	5.49	1.91	2.76
22	22.20	3.16	2.12	2.53
23	21.50	2.90	2.24	2.44
24	18.00	4.00	2.24	3.25
24.46	15.60	4.41	2.86	3.84
25	4.00	3.31	−0.21	4.02
		Z = 4.5 mm (radial scan)		
0	1.70	4.30	−0.08	1.57
2	1.94	4.29	0.16	1.52
4	3.07	3.98	0.46	1.28
6	4.22	3.65	0.82	1.03
8	4.80	3.14	1.22	0.88
10	5.47	3.25	1.69	0.86
11	5.62	2.97	2.01	0.89
12	5.79	3.02	2.29	1.11
13	4.50	2.68	3.17	1.41
14	1.51	2.38	2.84	1.83

(Continued)

Table B1 Axial (*Vz*) and radial (*Vr*) entrance velocity mean and rms as a function of position in the methane flame (continued)

r, mm	Vz, m/s	$VzRMS$, m/s	Vr, m/s	$VrRMS$, m/s
14.38	−0.09	2.58	2.48	1.90
14.69	−0.96	2.77	2.06	2.06
15	−1.83	2.75	1.59	2.05
15.46	0.33	4.21	0.53	2.82
16	10.60	6.50	0.18	2.54
17	22.00	4.81	2.14	1.72
18	24.80	3.35	2.59	1.69
20	25.80	2.83	2.51	2.09
22	25.90	2.96	2.44	2.26
24	24.90	3.33	2.47	2.24
24.46	23.60	3.51	2.33	2.45
25	21.20	4.05	2.42	2.63

Table B2 Axial (*Vz*) and azimuthal (Vθ) entrance velocity mean and rms as a function of position in the methane flame

r, mm	Vz, m/s	$VzRMS$, m/s	$V\theta$, m/s	$V\theta RMS$, m/s
0	2.08	4.20	−0.02	1.50
2	2.55	4.21	0.62	1.49
4	3.45	3.82	1.11	1.24
6	4.28	3.49	1.43	0.98
8	4.85	3.15	1.55	0.80
10	5.35	2.98	1.59	0.70
11	5.59	3.01	1.62	0.70
12	5.79	3.03	1.68	0.77
13	5.51	2.99	1.66	0.93
14	2.34	2.48	1.70	1.28
15	−2.51	2.66	1.88	2.02
16	8.77	6.28	4.94	3.21
17	18.90	4.90	8.83	2.43
18	23.30	3.85	11.50	1.88
20	26.00	2.83	14.00	1.56
22	25.80	2.87	14.80	1.67
24	24.90	3.18	15.20	2.22
25	22.00	4.28	13.30	3.62
26	7.82	4.72	9.07	3.88
27	1.74	1.99	7.03	2.68
28	1.44	1.63	6.95	2.47
30	1.11	1.54	7.01	2.35
35	0.77	1.66	6.68	2.28
40	0.62	1.89	6.37	2.23
50	−0.06	2.61	5.67	2.42
60	−0.93	4.13	5.20	2.77

Table B3 Axial (*Vz*) and azimuthal (Vθ) velocity mean and rms as a function of position in the methane flame

r, mm	Vz, m/s	$VzRMS$, m/s	$V\theta$, m/s	$V\theta RMS$, m/s
		$Z = 43.8$ *mm*		
−60	−6.97	7.36	−4.80	5.78
−50	3.20	7.74	−6.65	5.86
−40	14.96	6.92	−7.47	4.83
−30	23.58	8.92	−9.02	4.66
−20	18.43	13.11	−10.37	6.11
−10	−4.56	12.70	−6.68	6.67
0	−14.46	10.53	−0.76	5.26
10	−7.72	12.05	5.22	6.27
20	17.44	14.92	9.56	6.49
30	25.60	8.73	9.16	4.51
40	17.75	6.05	7.65	4.60
50	6.49	7.94	7.33	5.49
60	−6.21	7.30	7.43	5.59
		$Z = 79.6$ *mm*		
−60	4.52	11.16	−4.31	6.22
−50	14.33	7.63	−5.42	5.46
−40	17.26	8.33	−6.63	5.00
−30	14.86	10.39	−7.35	4.93
−20	5.52	11.59	−6.96	5.20
−10	−4.76	9.15	−3.34	5.35
0	−9.27	7.17	−0.29	4.98
10	−8.77	7.01	3.13	4.82
20	−1.50	10.82	5.88	5.46
30	9.24	13.04	6.53	5.36
40	17.70	9.96	6.14	5.10
50	16.76	7.82	5.74	5.06
60	8.13	10.18	6.05	5.61
		$Z = 115.3$ *mm*		
−60	12.67	5.88	−4.09	4.37
−50	13.22	5.48	−4.34	4.26
−40	11.33	6.50	−4.66	4.29
−30	6.64	7.48	−4.80	4.41
−20	0.83	7.01	−4.27	4.40
−10	−3.28	5.45	−2.80	4.34
0	−5.06	4.29	−0.22	4.26
10	−4.45	4.61	2.63	4.35
20	−2.28	5.43	4.61	4.42
30	2.25	7.01	5.39	4.29
40	8.48	7.39	5.34	4.53
50	13.87	6.18	5.08	4.25
60	16.27	5.64	5.30	4.07
		$Z = 151.8$ *mm*		
−60	15.35	4.51	−4.16	3.30
−50	13.01	4.59	−4.52	3.52
−40	9.78	5.15	−4.63	3.76
−30	6.28	5.32	−4.77	3.77
−20	2.94	5.21	−4.29	3.77
−10	0.71	4.81	−2.82	3.75
0	−1.15	4.33	−0.35	3.94
10	−1.01	4.26	2.35	3.75
20	0.88	4.76	4.29	3.77
30	3.93	5.48	5.28	3.76
40	8.04	5.50	5.23	3.82
50	12.54	4.71	4.83	3.63
60	16.94	4.46	4.85	3.29
		$Z = 187.6$ *mm*		
−60	15.48	4.35	−4.31	2.75
−50	13.28	4.31	−4.64	3.01
−40	10.75	4.28	−4.66	3.15
−30	8.24	4.24	−4.73	3.17
−20	5.91	4.43	−4.09	3.15
−10	3.86	4.42	−2.41	3.41
0	2.91	4.41	−0.49	3.59
10	3.12	4.69	1.59	3.34
20	4.33	4.34	3.64	3.38
30	6.40	4.67	4.84	3.29
40	9.44	4.70	4.98	3.29
50	12.89	4.36	4.91	3.29
60	16.25	4.28	4.82	2.91
		$Z = 304$ *mm*		
−60	13.88	4.52	−5.16	2.34
−50	12.85	4.04	−5.19	2.59
−40	11.48	3.48	−4.67	2.37
−30	10.28	3.57	−4.35	2.46
−20	8.71	3.42	−3.14	2.69
−10	7.73	3.16	−2.01	2.65
0	7.52	3.58	−0.34	2.67
10	7.20	3.27	1.30	3.03
20	8.19	3.82	3.45	2.78
30	9.12	3.69	4.54	2.90
40	10.96	4.27	5.47	3.02
50	12.69	3.56	5.29	3.13
60	13.58	3.26	5.03	2.89
		$Z = 325$ *mm*		
−60	13.44	4.53	−5.28	2.11
−50	12.93	3.95	−5.24	2.13
−40	11.73	4.12	−5.05	2.18
−30	10.60	3.74	−4.28	2.17
−20	9.79	3.68	−3.07	2.68
−10	9.28	3.81	−1.51	2.95
0	8.64	3.69	0.35	3.03
10	8.78	3.74	2.09	2.88
20	9.09	4.01	3.68	2.65
30	10.47	3.97	4.89	2.43
40	11.69	4.49	5.40	2.38
50	12.60	4.49	5.13	2.40
60	12.69	4.35	4.96	2.43

Table B4 Axial (Vz) and azimuthal ($V\theta$) entrance velocity mean and rms as a function of position in the cold flow

r, mm	Vz, m/s	$VzRMS$, m/s	$V\theta$, m/s	$V\theta RMS$, m/s
		Z = 4.5 mm		
0	2.76	1.21	−0.85	1.42
1	2.79	1.16	−0.66	1.39
2	2.83	1.17	−0.44	1.40
3	2.90	1.19	−0.24	1.37
4	2.96	1.16	−0.02	1.28
5	3.04	1.13	0.21	1.17
6	3.11	1.13	0.38	1.07
7	3.17	1.12	0.51	0.97
8	3.28	1.08	0.60	0.91
9	3.40	1.11	0.65	0.86
10	3.56	1.15	0.72	0.82
11	3.73	1.22	0.73	0.83
12	3.93	1.29	0.78	0.82
13	4.06	1.35	0.74	0.95
14	0.76	0.87	0.05	1.90
15	0.09	0.77	0.14	2.58
15.5	−0.73	0.98	0.10	2.30
15.8	−1.24	1.22	0.11	2.10
16	−1.51	1.50	0.27	1.98
16.2	1.35	3.97	1.18	2.36
16.5	3.92	4.77	1.85	2.48
17	18.05	2.79	7.25	2.06
18	21.41	2.04	10.02	1.75
19	22.94	1.53	12.26	1.57
20	23.39	1.38	13.69	1.51
21	23.29	1.41	14.49	1.54
22	22.75	1.51	14.94	1.66
23	22.21	1.73	15.24	1.85
24	21.48	2.08	15.42	2.21
25	18.39	3.92	13.91	3.70
25.5	14.15	4.96	11.64	4.54
26	6.91	4.32	9.51	4.41
27	1.02	1.82	8.76	3.53
28	0.60	1.53	8.88	3.12
29	0.39	1.43	8.76	2.97
30	0.25	1.41	8.59	2.81
33	0.06	1.41	8.08	2.51
36	−0.05	1.45	7.66	2.33
39	−0.06	1.44	7.21	2.17

Table B5 Axial (Vz) and azimuthal ($V\theta$) velocity mean and rms as a function of position in the cold flow

r, mm	Vz, m/s	$VzRMS$, m/s	$V\theta$, m/s	$V\theta RMS$, m/s
		Z = 38.1 mm		
−66.3	−4.39	4.77	−4.24	3.48
−63.5	−3.15	4.30	−4.30	3.58
−50.8	3.69	4.46	−5.65	3.05
−38.1	13.35	6.85	−6.73	4.52
−31.8	7.11	7.31	−9.25	4.92
−25.4	2.70	8.65	−3.42	4.81
−12.7	0.12	6.11	−2.42	3.86
0.0	−3.80	4.27	0.85	2.68
12.7	−2.19	5.05	2.74	2.55
25.4	14.33	8.45	7.73	5.79
38.1	9.98	5.35	5.14	4.09
50.8	1.73	3.72	4.42	2.68
63.5	−2.67	3.80	4.40	3.40
67.6	−4.05	4.30	4.92	3.05
70.1	−5.38	4.62	4.37	3.20
		Z = 152.4 mm		
−65.8	5.25	2.86	−4.55	2.33
−63.5	5.57	2.83	−4.67	2.28
−50.8	2.66	2.90	−4.95	2.32
−38.1	0.26	2.45	−5.18	2.14
−25.4	−0.37	2.32	−6.07	2.40
−12.7	−0.28	2.81	−6.02	3.09
−9.5	0.03	3.19	−5.26	3.64
−6.4	0.26	3.30	−4.11	4.25
−3.2	0.52	3.61	−2.28	4.97
0.0	0.57	3.48	−0.14	5.07
3.2	0.77	3.59	2.02	5.05
6.4	0.55	3.49	4.09	4.30
9.5	0.09	3.12	5.24	3.74
12.7	0.00	2.83	5.99	3.26
25.4	−0.22	2.33	6.18	2.48
38.1	−0.09	2.32	5.07	2.20
50.8	2.02	2.92	4.83	2.41
63.5	4.85	3.25	4.25	2.49
69.9	4.79	3.58	3.75	2.58
		Z = 190.5 mm		
−65.5	2.47	2.78	−4.95	1.87
−63.0	4.44	3.55	−4.30	2.14
−57.2	2.42	2.44	−4.87	1.79
−50.8	2.20	2.45	−4.81	1.76
−38.1	1.52	2.30	−4.88	1.85
−25.4	0.81	1.94	−4.16	2.06
−12.7	1.00	2.53	−5.60	3.01
0.0	2.58	3.31	−0.61	4.65
		Z = 228.6 mm		
−69.7	1.16	1.75	−4.19	1.53
−65.7	1.73	2.04	−4.70	1.47
−63.1	2.85	2.82	−4.64	1.66
−50.4	2.48	2.58	−4.44	1.73
−37.7	2.05	1.79	−5.10	1.45
−25.0	1.91	1.84	−6.00	1.59
−12.3	2.01	2.22	−5.82	2.51
0.4	2.31	2.10	−1.03	2.61
6.7	3.70	2.73	4.04	3.73
		Z = 304 mm		
−63.5	1.84	1.35	−4.88	1.00
−50.8	1.83	1.23	−4.86	0.97
−38.1	1.79	1.28	−5.06	1.07
−25.4	1.94	1.44	−5.37	1.18
−12.7	2.84	1.81	−5.77	2.57
−6.4	4.24	2.12	−4.85	4.05
0.0	6.07	3.08	−2.56	4.98
6.4	5.98	3.22	3.58	4.61
12.7	4.03	2.21	6.31	3.32
25.4	2.02	1.49	5.88	1.48
38.1	1.85	1.32	5.25	1.08
50.8	1.91	1.25	4.96	0.98
63.5	2.00	1.42	4.97	1.00
		Z = 325 mm		
−67.1	1.77	1.23	−4.73	1.14
−63.5	1.87	1.11	−4.67	0.89
−50.8	1.66	1.06	−4.77	0.87
−38.1	1.53	1.11	−5.06	0.89
−25.4	1.73	1.25	−5.44	1.06
−12.7	3.04	1.73	−5.98	2.43
−6.4	4.76	2.20	−5.66	4.02
0.0	6.42	2.79	−2.25	5.03
6.4	6.22	2.82	4.40	4.62
12.7	4.12	2.02	6.77	3.15
25.4	2.00	1.32	5.77	1.39
38.1	1.72	1.16	5.14	0.93
50.8	1.84	1.06	4.84	0.84
63.5	2.06	1.23	4.76	0.89
69.6	1.78	1.31	4.60	1.00

Table B6 Mean temperature as a function of position in the methane flame (uncoated bead, radiation corrected)

	$Z = 7.3$ mm		$Z = 25.6$ mm		$Z = 43.8$ mm		$Z = 61.3$ mm		$Z = 79.6$ mm		$Z = 97.8$ mm		$Z = 115.3$ mm		$Z = 133.6$ mm		$Z = 151.8$ mm		$Z = 187.6$ mm		$Z = 223.4$ mm		$Z = 259.9$ mm	
r, mm	T, K	±	T, K	±	T, K	±	T, K	±	T, K	±	T, K	±	T, K	±	T, K	±	T, K	±	T, K	±	T, K	±	T, K	±
65	912	21	1037	21	1121	21	1166	21	1142	31	1217	31	1334	31	1423	31	1411	31	1418	31	1412	31	1378	31
60	1001	21	1112	21	1175	21	1164	21	1197	31	1395	34	1507	35	1507	35	1506	35	1519	32	1519	32	1466	31
55	1017	21	1144	21	1186	21	1119	21	1270	34	1558	37	1655	37	1618	35	1644	35	1576	32	1558	32	1552	32
50	1043	21	1155	21	1153	21	1044	32	1402	37	1718	38	1709	38	1718	35	1675	32	1635	32	1604	32	1610	32
45	1032	21	1109	21	1054	32	1049	30	1529	37	1747	38	1771	36	1732	33	1707	32	1659	32	1640	32	1640	32
40	1026	21	1092	26	847	43	1153	34	1625	35	1770	33	1782	33	1755	33	1722	33	1704	32	1671	32	1658	32
35	1014	21	1017	26	649	52	1378	43	1722	35	1788	33	1802	43	1780	42	1752	33	1724	33	1677	32	1670	32
30	998	17	725	22	790	58	1563	43	1735	33	1819	43	1814	43	1788	52	1763	42	1718	33	1697	33	1690	33
25	856	16	388	21	1189	59	1668	46	1817	42	1831	43	1818	43	1772	52	1756	52	1726	52	1705	52	1678	52
20	323	16	493	16	1539	44	1795	54	1852	52	1861	62	1829	62	1793	52	1750	52	1729	52	1715	52	1701	52
15	308	11	957	26	1646	37	1838	54	1867	52	1867	62	1837	62	1793	62	1728	52	1714	52	1707	52	1700	52
10	323	11	1112	26	1731	33	1864	52	1881	52	1866	62	1829	62	1786	62	1728	52	1714	52	1693	52	1686	52
5	333	11	1323	26	1746	33	1877	52	1874	52	1859	62	1837	62	1793	62	1736	52	1700	52	1679	52	1679	52
0	358	16	1391	27	1756	33	1891	52	1874	52	1859	62	1838	62	1786	62	1736	52	1693	52	1686	52	1672	52

Table B7 Carbon dioxide as a function of position in the methane flame (mole percentage, measured on a dry basis)

	$Z = 7.3$ mm		$Z = 25.6$ mm		$Z = 43.8$ mm		$Z = 61.3$ mm		$Z = 79.6$ mm		$Z = 97.8$ mm		$Z = 115.3$ mm		$Z = 133.6$ mm		$Z = 151.8$ mm		$Z = 187.6$ mm		$Z = 223.4$ mm		$Z = 259.9$ mm	
r, mm	CO_2, %	±	CO_2, %	±	CO_2, %	±	CO_2, %	±	CO_2, %	±	CO_2, %	±	CO_2, %	±	CO_2, %	±	CO_2, %	±	CO_2, %	±	CO_2, %	±	CO_2, %	±
65	3.85	0.39	2.87	0.29	3.85	0.39	2.98	0.30	3.35	0.33	4.26	0.43	4.82	0.48	5.42	0.54	5.42	0.54	5.90	0.59	6.24	0.62	6.57	0.66
60	4.12	0.41	2.87	0.29	4.12	0.41	3.24	0.32	3.24	0.32	4.97	0.50	5.58	0.56	5.90	0.59	5.90	0.59	6.24	0.62	6.57	0.66	6.75	0.68
55	3.99	0.40	3.11	0.31	3.99	0.40	3.24	0.32	3.24	0.32	5.58	0.56	6.24	0.62	6.57	0.66	6.24	0.62	6.57	0.66	6.92	0.69	6.92	0.69
50	3.99	0.40	3.73	0.75	2.10	0.42	2.87	0.57	3.48	0.35	6.40	0.64	6.92	0.69	7.11	0.71	6.92	0.69	7.11	0.71	7.11	0.71	7.11	0.71
45	3.85	0.77	3.73	0.75	2.98	0.30	2.76	0.28	4.40	0.44	7.11	0.71	7.48	0.75	7.48	0.75	7.11	0.71	7.30	0.73	7.30	0.73	6.92	0.69
40	3.73	0.75	3.85	0.77	1.99	0.20	2.98	0.30	5.27	0.53	7.88	0.79	7.88	0.79	7.68	0.77	7.48	0.75	7.48	0.75	7.30	0.73	7.30	0.73
35	3.99	0.80	3.24	0.65	1.01	0.10	4.12	0.41	6.57	0.66	8.48	0.85	8.07	0.81	8.27	0.83	7.88	0.79	7.48	0.75	7.68	0.77	7.48	0.75
30	3.60	0.36	1.01	0.20	1.39	0.14	5.58	0.56	6.92	0.69	8.48	0.85	8.27	0.83	8.27	0.83	8.07	0.81	7.68	0.77	7.68	0.77	7.48	0.75
25	0.29	0.10	0.13	0.10	3.24	0.32	6.40	0.64	8.27	0.83	8.69	0.87	8.69	0.87	8.69	0.87	8.27	0.83	7.88	0.79	7.68	0.77	7.30	0.73
20	0.00	0.10	0.46	0.10	4.97	0.50	7.88	0.79	8.48	0.85	9.11	0.91	8.69	0.87	8.90	0.89	8.27	0.83	8.07	0.81	7.88	0.79	7.68	0.77
15	0.00	0.10	1.89	0.19	6.40	0.64	8.48	0.85	8.48	0.85	9.11	0.91	8.69	0.87	8.90	0.89	8.27	0.83	7.88	0.79	7.88	0.79	7.88	0.79
10	0.00	0.10	1.99	0.20	7.30	0.73	8.27	0.83	8.90	0.89	9.11	0.91	8.48	0.85	8.69	0.87	8.48	0.85	8.27	0.83	7.88	0.79	7.88	0.79
5	0.00	0.10	2.20	0.22	7.68	0.77	8.90	0.89	9.11	0.91	9.33	0.93	8.48	0.85	8.90	0.89	8.27	0.83	8.07	0.81	7.88	0.79	7.68	0.77
0	0.00	0.10	2.87	0.29	7.68	0.77	8.27	0.83	9.11	0.91	9.11	0.91	8.69	0.87	8.69	0.87	8.27	0.83	8.27	0.83	8.07	0.81	7.48	0.75

Table B8 Oxygen as a function of position in the methane flame (mole percentage, measured on a dry basis)

	$Z = 7.3$ mm		$Z = 25.6$ mm		$Z = 43.8$ mm		$Z = 61.3$ mm		$Z = 79.6$ mm		$Z = 97.8$ mm		$Z = 115.3$ mm		$Z = 133.6$ mm		$Z = 151.8$ mm		$Z = 187.6$ mm		$Z = 223.4$ mm		$Z = 259.9$ mm	
r, mm	O_2, %	±	O_2, %	±	O_2, %	±	O_2, %	±	O_2, %	±	O_2, %	±	O_2, %	±	O_2, %	±	O_2, %	±	O_2, %	±	O_2, %	±	O_2, %	±
65	13.80	1.38	14.10	1.41	13.50	1.35	13.60	1.36	13.10	1.31	12.60	1.00	11.10	1.00	10.50	1.00	9.30	0.93	8.90	0.89	8.60	0.86	8.60	0.86
60	13.80	1.38	13.70	1.37	13.10	1.31	13.70	1.37	12.90	1.29	11.90	1.00	9.90	0.99	9.50	0.95	8.80	0.88	8.30	0.83	8.10	0.81	8.30	0.83
55	13.20	1.32	13.90	1.39	13.30	1.33	14.00	1.40	12.40	1.24	11.20	1.00	8.60	0.86	8.30	0.83	8.10	0.81	7.90	0.79	7.70	0.77	8.00	0.80
50	13.30	1.33	13.80	1.38	13.90	1.39	14.50	1.45	10.60	1.06	9.30	0.93	7.30	0.73	7.40	0.74	7.40	0.74	7.90	0.79	7.50	0.75	7.50	0.75
45	13.40	1.34	14.00	1.40	14.80	1.48	14.60	2.92	9.90	0.99	8.00	0.80	6.40	0.64	6.70	0.67	6.80	0.68	7.20	0.72	7.40	0.74	7.60	0.76
40	13.20	1.32	14.30	1.43	16.40	1.64	13.20	2.64	7.70	0.77	6.50	0.65	5.30	0.53	6.00	0.60	6.20	0.62	6.60	0.66	6.90	0.69	7.10	0.71
35	13.70	1.37	15.40	1.54	17.80	3.56	10.30	2.06	6.40	0.64	4.80	0.48	4.50	0.45	5.40	0.54	5.60	0.56	6.10	0.61	6.70	0.67	6.90	0.69
30	13.80	2.76	19.50	3.90	16.10	3.22	7.70	1.54	5.10	0.51	4.40	0.44	4.00	0.40	4.80	0.48	5.10	0.51	6.10	0.61	6.40	0.64	6.90	0.69
25	20.90	4.18	20.30	4.06	11.60	2.32	5.30	1.06	3.70	0.37	3.70	0.37	3.90	0.39	4.50	0.45	5.10	0.51	5.80	0.58	6.40	0.64	6.60	0.66
20	21.00	4.20	15.20	3.04	7.60	1.52	3.70	0.74	3.50	0.35	3.60	0.36	3.90	0.39	4.50	0.45	5.00	0.50	5.70	0.57	6.10	0.61	6.70	0.67
15	5.30	1.06	9.70	1.94	5.50	1.10	3.30	0.33	3.10	0.31	3.40	0.34	3.80	0.38	4.40	0.44	4.90	0.49	5.50	0.55	6.00	0.60	6.50	0.65
10	1.30	0.26	8.70	1.74	3.50	0.70	3.30	0.33	3.20	0.32	3.60	0.36	3.80	0.38	4.40	0.44	5.00	0.50	5.60	0.56	5.90	0.59	6.40	0.64
5	0.40	0.10	7.60	1.52	3.20	0.32	3.30	0.33	3.30	0.33	3.60	0.36	4.00	0.40	4.40	0.44	5.00	0.50	5.60	0.56	6.10	0.61	6.30	0.63
0	0.30	0.10	4.70	0.47	3.70	0.37	3.50	0.35	3.50	0.35	3.60	0.36	4.00	0.40	4.50	0.45	5.00	0.50	5.40	0.54	5.90	0.59	6.30	0.63

Table B9 Carbon monoxide as a function of position in the methane flame (mole percentage, measured on a dry basis)

	$Z = 7.3$ mm		$Z = 25.6$ mm		$Z = 43.8$ mm		$Z = 61.3$ mm		$Z = 79.6$ mm		$Z = 97.8$ mm		$Z = 115.3$ mm		$Z = 133.6$ mm		$Z = 151.8$ mm		$Z = 187.6$ mm		$Z = 223.4$ mm		$Z = 259.9$ mm	
r, mm	CO, %	±	CO, %	±	CO, %	±	CO, %	±	CO, %	±	CO, %	±	CO, %	±	CO, %	±	CO, %	±	CO, %	±	CO, %	±	CO, %	±
65	0.41	0.20	0.44	0.20	0.46	0.20	0.47	0.20	0.64	0.10	0.81	0.10	0.76	0.10	0.68	0.10	0.54	0.10	0.38	0.10	0.27	0.10	0.17	0.10
60	0.40	0.20	0.44	0.20	0.43	0.20	0.47	0.20	0.64	0.10	0.93	0.19	0.85	0.17	0.68	0.10	0.57	0.10	0.38	0.10	0.27	0.10	0.17	0.10
55	0.38	0.20	0.43	0.20	0.42	0.20	0.46	0.20	0.72	0.10	1.02	0.20	0.93	0.19	0.76	0.10	0.57	0.10	0.41	0.10	0.31	0.10	0.18	0.10
50	0.37	0.20	0.41	0.20	0.38	0.20	0.51	0.20	0.98	0.20	1.13	0.23	0.98	0.20	0.81	0.10	0.59	0.10	0.38	0.10	0.25	0.10	0.14	0.10
45	0.35	0.20	0.38	0.20	0.35	0.20	0.65	0.20	1.13	0.23	1.22	0.24	0.98	0.20	0.81	0.10	0.64	0.10	0.38	0.10	0.24	0.10	0.11	0.10
40	0.35	0.20	0.36	0.20	0.32	0.20	1.00	0.20	1.22	0.24	1.26	0.25	1.02	0.20	0.89	0.10	0.68	0.10	0.33	0.10	0.23	0.10	0.11	0.10
35	0.34	0.20	0.31	0.20	0.38	0.20	1.42	0.30	1.30	0.26	1.26	0.25	1.02	0.20	0.85	0.10	0.59	0.10	0.37	0.10	0.17	0.10	0.08	0.10
30	0.35	0.20	0.14	0.20	0.65	0.20	1.95	0.50	1.34	0.27	1.22	0.24	1.02	0.20	0.85	0.10	0.54	0.10	0.28	0.10	0.18	0.10	0.10	0.10
25	0.04	0.20	0.12	0.20	1.42	0.30	1.75	0.50	1.26	0.25	1.13	0.23	0.89	0.18	0.64	0.10	0.57	0.10	0.27	0.10	0.16	0.10	0.08	0.10
20	0.00	0.20	0.39	0.20	2.17	0.50	1.58	0.40	1.26	0.25	1.02	0.20	0.85	0.17	0.89	0.10	0.48	0.10	0.23	0.10	0.11	0.10	0.06	0.10
15	0.00	0.20	1.00	0.20	2.17	0.50	1.27	0.30	1.17	0.23	0.89	0.18	0.64	0.10	0.48	0.10	0.35	0.10	0.21	0.10	0.10	0.10	0.04	0.10
10	0.00	0.20	1.42	0.30	2.52	0.50	1.27	0.30	1.02	0.20	0.81	0.10	0.59	0.10	0.37	0.10	0.27	0.10	0.17	0.10	0.07	0.10	0.04	0.10
5	0.00	0.20	1.42	0.30	1.95	0.50	1.00	0.30	0.98	0.20	0.57	0.10	0.51	0.10	0.37	0.10	0.24	0.10	0.11	0.10	0.07	0.10	0.03	0.10
0	0.00	0.20	1.75	0.30	1.95	0.50	1.13	0.20	0.93	0.19	0.54	0.10	0.45	0.10	0.38	0.10	0.23	0.10	0.10	0.10	0.06	0.10	0.03	0.10

Table B10 Hydrocarbons as a function of position in the methane flame (mole ppm, measured on a wet basis)

	$Z = 7.3$ mm		$Z = 43.8$ mm		$Z = 61.3$ mm		$Z = 97.8$ mm		$Z = 133.6$ mm		$Z = 187.6$ mm		$Z = 223.4$ mm		$Z = 259.9$ mm	
r, mm	HC	±	HC	±	HC	±	HC	±	HC	±	HC	±	HC	±	HC	±
65	1,714	171	4,862	972	——	——	9,231	923	4,260	426	1,880	188	1,110	111	684	68
60	——	——	——	——	5,669	1,134	——	——	——	——	——	——	——	——	——	——
55	1,297	130	4,800	960	——	——	8,847	885	1,696	170	778	78	430	43	289	29
50	——	——	——	——	9,314	1,863	——	——	——	——	——	——	——	——	——	——
45	1,306	131	6,737	1,347	——	——	6,658	666	856	86	310	31	250	25	106	11
40	——	——	——	——	25,311	10,125	——	——	——	——	——	——	——	——	——	——
35	1,088	109	28,000	5,600	——	——	2,462	246	1,533	153	116	12	59	6	39	5
30	——	——	——	——	33,600	13,440	——	——	——	——	——	——	——	——	——	——
25	10	5	88,000	35,200	——	——	744	74	194	19	64	6	19	5	11	5
20	——	——	65,000	26,000	14,961	5,984	——	——	——	——	——	——	——	——	——	——
15	——	——	28,000	11,200	——	——	89	9	41	10	15	5	9	5	4	5
10	——	——	——	——	358	143	——	——	——	——	——	——	——	——	——	——
5	——	——	5,719	2,288	——	——	44	5	28	10	10	5	0	5	0	5
0	——	——	1,519	304	155	31	18	5	24	10	8	5	0	5	0	5

Table B11 Nitric oxide as a function of position in the methane flame (mole ppm measured on a dry basis)

	$Z = 25.6$ mm		$Z = 43.8$ mm		$Z = 61.3$ mm		$Z = 79.6$ mm		$Z = 97.8$ mm		$Z = 115.3$ mm		$Z = 133.6$ mm		$Z = 151.8$ mm		$Z = 187.6$ mm		$Z = 223.4$ mm		$Z = 259.9$ mm	
r, mm	NO	±	NO	±	NO	±	NO	±	NO	±	NO	±	NO	±	NO	±	NO	±	NO	±	NO	±
65	3.69	1.00	4.06	1.00	2.08	1.00	4.18	1.00	3.55	1.00	3.53	1.00	4.49	1.00	5.47	1.00	7.04	1.00	12.31	1.23	13.60	1.36
55	3.39	1.00	3.38	1.00	1.78	1.00	4.05	1.00	4.69	1.00	5.82	0.58	8.40	0.84	9.65	1.00	12.71	1.27	17.58	1.76	18.90	1.89
45	3.38	1.00	2.63	1.00	3.05	1.00	7.10	1.00	14.27	1.43	14.44	1.44	15.94	1.59	17.37	1.74	19.47	1.95	24.12	2.41	23.00	2.30
35	3.28	1.00	1.49	1.00	6.66	1.00	17.00	1.70	25.78	2.58	26.89	2.69	25.29	2.53	25.61	2.56	26.24	2.62	28.92	2.89	27.76	2.78
30	——	——	——	——	14.97	2.99	——	——	——	——	——	——	——	——	——	——	——	——	——	——	——	——
25	1.18	1.00	3.17	1.00	24.89	4.98	30.27	3.03	34.95	3.49	34.61	3.46	32.76	3.28	31.33	3.13	31.03	3.10	30.81	3.08	30.16	3.02
20	——	——	11.23	2.25	——	——	——	——	——	——	——	——	——	——	——	——	——	——	——	——	——	——
15	1.54	1.00	21.28	4.26	42.34	8.47	38.44	3.84	39.24	3.92	38.90	3.89	35.91	3.59	35.20	3.52	33.86	3.39	33.04	3.30	31.73	3.17
5	2.86	1.00	30.90	3.09	42.81	4.28	40.87	4.09	40.27	4.03	39.50	3.95	36.84	3.68	36.24	3.62	35.65	3.57	34.98	3.50	33.12	3.31
0	2.91	1.00	33.61	3.36	43.15	4.31	40.12	4.01	41.26	4.13	39.75	3.98	37.76	3.78	36.63	3.66	36.13	3.61	35.34	3.53	34.60	3.46

Acknowledgment

This research was supported by the NASA Ultra-Efficient Engine Technologies program under Grant NAG2-1539, with Nagi Mansour as technical monitor.

References

[1] Heap, M. P., Lowes, T. M., and Walmsley, R., "Emission of Nitric Oxide from Large Turbulent Diffusion Flames," *Proceedings of the Fourteenth International Symposium on Combustion*, The Combustion Institute, Pittsburgh, PA, 1973, pp. 883–895.

[2] Owen, F. K., Spadaccini, L. J., Bowman, C. T., "Pollutant Formation and Energy Release in Confined Turbulent Diffusion Flames," *Proceedings of the Sixteenth International Symposium on Combustion*, The Combustion Institute, Pittsburgh, PA, 1977, pp. 105–117.

[3] Claypole, T. C., and Syred, N., "The Effect of Swirl Burner Aerodynamics on NO_x Formation," *Proceedings of the Eighteenth International Symposium on Combustion*, The Combustion Institute, Pittsburgh, PA, 1981, pp. 81–89.

[4] Starner, S. H., and Bilger, R. W., "Joint Measurement of Velocity and Scalars in a Turbulent Diffusion Flame with Moderate Swirl," *Proceedings of the Twenty-First International Symposium on Combustion*, The Combustion Institute, Pittsburgh, PA, 1986, pp. 1569–1577.

[5] Brum, R. D., and Samuelsen, G. S., "Two-Component Laser Anemometer Measurement of Non-Reacting and Reacting Complex Flows in a Swirl-Stabilized Model Combustor," *Experiments in Fluids*, Vol. 5, No. 1, 1987, pp. 95–102.

[6] Charles, R. E., and Samuelsen, G. S., "An Experimental Data Base for the Computational Fluid Dynamics of Combustors," *Journal of Engineering for Gas Turbines and Power*, Vol. 111, No. 1, 1989, pp. 11–14.

[7] Tacke, M. M., Cheng, T. C., Hassel, E. P., and Janicka, J., "Study of Swirling Recirculating Hydrogen Diffusion Flame Using UV Raman Spectroscopy," *Proceedings of the Twenty-Sixth International Symposium on Combustion*, The Combustion Institute, Pittsburgh, PA, 1996, pp. 169–175.

[8] Landenfeld, T., Kremer, A., Hassel, E. P., Janika, J., Schäfer, T., Kazenwadel, J., Schulz, C., and Wolfrum, J., "Laser Diagnostic and Numerical Study of Strongly Swirling Natural Gas Flames," *Proceedings of the Twenty-Seventh International Symposium on Combustion*, The Combustion Institute, Pittsburgh, PA, 1998, pp. 1023–1029.

[9] Schmittel, P., Günther, B., Lenze, B., Leuckel, W., and Bockhorn, H., "Turbulent Swirling Flames: Experimental Investigation of the Flow Field and Formation of Nitrogen Oxide," *Proceedings of the Twenty-Eighth International Symposium on Combustion*, The Combustion Institute, Pittsburgh, PA, 2000, pp. 303–309.

[10] Kalt, P. A. M., Al-Abdelhi, Y. M., Masri, A. R., and Barlow, R. S., "Swirling Turbulent Non-Premixed Flames of Methane: Flowfield and Compositional Structure," *Proceedings of the Twenty-Ninth International Symposium on Combustion*, The Combustion Institute, Pittsburgh, PA, 2002, pp. 1913–1919.

[11] Bowman, C. T., "Gas-Phase Reaction Mechanisms for Nitrogen Oxide Formation and Removal in Combustion," *Pollutants from Combustion*, edited by C. Vovelle, Kluwer Academic, Amsterdam, 2000, pp. 123–144.

[12] Swithenbank, J., "Ecological Aspects of Combustion Devices with Reference to Hydrocarbon Flaring," *AICHE Journal*, Vol. 18, No. 3, 1972, pp. 553–560.